Research Article Vol. 25, No. 1 | 9 Jan 2017 | OPTICS EXPRESS 377

Optics EXPRESS

Spin-to-orbital angular momentum conversion in dielectric metasurfaces

Robert Charles Devlin,[1,6] **Antonio Ambrosio,**[1,2,3,6,7] **Daniel Wintz,**[1] **Stefano Luigi Oscurato,**[4] **Alexander Yutong Zhu,**[1] **Mohammadreza Khorasaninejad,**[1] **Jaewon Oh,**[1,5] **Pasqualino Maddalena,**[4] **and Federico Capasso**[1,8]

[1]*Harvard John A. Paulson School of Engineering and Applied Sciences, Harvard University, Cambridge, Massachusetts 02138, USA*
[2]*Center for Nanoscale Systems, Harvard University, Cambridge, Massachusetts 02138, USA*
[3]*CNR-SPIN U.O.S. Napoli, Complesso Universitario di Monte Sant'Angelo, Via Cintia, 80126 – Napoli, Italy*
[4]*Dipartimento di Fisica "E. Pancini", Università di Napoli Federico II, Complesso Universitario di Monte Sant'Angelo, Via Cintia, 80126 – Napoli, Italy*
[5]*University of Waterloo, Waterloo, ON N2L 3G1, Canada*
[6]*These authors contributed equally to this work*
[7]*ambrosio@seas.harvard.edu*
[8]*capasso@seas.harvard.edu*

Abstract: Vortex beams are characterized by a helical wavefront and a phase singularity point on the propagation axis that results in a doughnut-like intensity profile. These beams carry orbital angular momentum proportional to the number of intertwined helices constituting the wavefront. Vortex beams have many applications in optics, such as optical trapping, quantum optics and microscopy. Although beams with such characteristics can be generated holographically, spin-to-orbital angular momentum conversion has attracted considerable interest as a tool to create vortex beams. In this process, the geometrical phase is exploited to create helical beams whose handedness is determined by the circular polarization (left/right) of the incident light, that is by its spin. Here we demonstrate high-efficiency Spin-to-Orbital angular momentum-Converters (SOCs) at visible wavelengths based on dielectric metasurfaces. With these SOCs we generate vortex beams with high and fractional topological charge and show for the first time the simultaneous generation of collinear helical beams with different and arbitrary orbital angular momentum. This versatile method of creating vortex beams, which circumvents the limitations of liquid crystal SOCs and adds new functionalities, should significantly expand the applications of these beams.

OCIS codes: (350.1370) Berry's phase; (230.0230) Optical devices.

References and links

1. J. F. Nye and M. V. Berry, "Dislocations in wave train," Proc. R. Soc. Lond. A Math. Phys. Sci. **336**(1605), 165–190 (1974).
2. L. Allen, M. W. Beijersbergen, R. J. C. Spreeuw, and J. P. Woerdman, "Orbital angular momentum of light and the transformation of Laguerre-Gaussian laser modes," Phys. Rev. A **45**(11), 8185–8189 (1992).
3. A. Mair, A. Vaziri, G. Weihs, and A. Zeilinger, "Entanglement of the orbital angular momentum states of photons," Nature **412**(6844), 313–316 (2001).
4. M. R. Dennis, K. O'Holleran, and M. J. Padgett, "Singular Optics: Optical Vortices and Polarization Singularities," Prog. Opt. **53**, 293–363 (2009).
5. M. J. Padgett and R. Bowman, "Tweezers with a twist," Nat. Photonics **5**(6), 343–348 (2011).
6. M. E. J. Friese, J. Enger, H. Rubinsztein-Dunlop, and N. R. Heckenberg, "Optical angular-momentum transfer to trapped absorbing particles," Phys. Rev. A **54**(2), 1593–1596 (1996).
7. N. B. Simpson, K. Dholakia, L. Allen, and M. J. Padgett, "Mechanical equivalence of spin and orbital angular momentum of light: an optical spanner," Opt. Lett. **22**(1), 52–54 (1997).
8. A. Ambrosio, B. Piccirillo, A. Sasso, and E. Santamato, "Experimental and theoretical study of the transient rotation of isotropic transparent microparticles in astigmatic optical tweezers," Opt. Commun. **230**(4-6), 337–

#278547 http://dx.doi.org/10.1364/OE.25.000377
Journal © 2017 Received 24 Oct 2016; revised 21 Dec 2016; accepted 21 Dec 2016; published 5 Jan 2017
Corrected: 11 January 2017

345 (2004).

9. J. Lin, P. Genevet, M. A. Kats, N. Antoniou, and F. Capasso, “Nanostructured holograms for broadband manipulation of vector beams,” Nano Lett. **13**(9), 4269–4274 (2013).
10. A. Ambrosio, L. Marrucci, F. Borbone, A. Roviello, and P. Maddalena, “Light-induced spiral mass transport in azo-polymer films under vortex-beam illumination,” Nat. Commun. **3**, 989 (2012).
11. G. Machavariani, N. Davidson, E. Hasman, S. Blit, A. A. Ishaaya, and A. A. Friesem, “Efficient conversion of a Gaussian beam to a high purity helical beam,” Opt. Commun. **209**(4-6), 265–271 (2002).
12. F. Bouchard, H. Mand, M. Mirhosseini, E. Karimi, and R. W. Boyd, “Achromatic orbital angular momentum generator,” New J. Phys. **16**(12), 123006 (2014).
13. S. Pancharatnam, “Generalized theory of interference, and its applications,” Proc. Ind. Acad. Sci. A **44**, 247 (1956).
14. M. V. Berry, “Quantal phase factors accompanying adiabatic changes,” Proc. R. Soc. Lond. A Math. Phys. Sci. **392**(1802), 45–57 (1984).
15. G. Milione, H. I. Sztul, D. A. Nolan, and R. R. Alfano, “Higher-order Poincaré sphere, stokes parameters, and the angular momentum of light,” Phys. Rev. Lett. **107**(5), 053601 (2011).
16. G. Biener, A. Niv, V. Kleiner, and E. Hasman, “Formation of helical beams by use of Pancharatnam-Berry phase optical elements,” Opt. Lett. **27**(21), 1875–1877 (2002).
17. A. Niv, G. Biener, V. Kleiner, and E. Hasman, “Spiral phase elements obtained by use of discrete space-variant subwavelength gratings,” Opt. Commun. **251**(4-6), 306–314 (2005).
18. E. Nagali, L. Sansoni, F. Sciarrino, F. De Martini, L. Marrucci, B. Piccirillo, E. Karimi, and E. Santamato, “Optimal quantum cloning of orbital angular momentum photon qubits through Hong–Ou–Mandel coalescence,” Nat. Photonics **3**(12), 720–723 (2009).
19. L. Marrucci, C. Manzo, and D. Paparo, “Pancharatnam-Berry phase optical elements for wave front shaping,” Appl. Phys. Lett. **88**(22), 221102 (2006).
20. G. Milione, M. P. J. Lavery, H. Huang, Y. Ren, G. Xie, T. A. Nguyen, E. Karimi, L. Marrucci, D. A. Nolan, R. R. Alfano, and A. E. Willner, “4 × 20 Gbit/s mode division multiplexing over free space using vector modes and a q-plate mode (de)multiplexer,” Opt. Lett. **40**(9), 1980–1983 (2015).
21. H. Huang, G. Milione, M. P. J. Lavery, G. Xie, Y. Ren, Y. Cao, N. Ahmed, T. An Nguyen, D. A. Nolan, M.-J. Li, M. Tur, R. R. Alfano, and A. E. Willner, “Mode division multiplexing using an orbital angular momentum mode sorter and MIMO-DSP over a graded-index few-mode optical fibre,” Sci. Rep. **5**, 14931 (2015).
22. N. Yu and F. Capasso, “Flat optics with designer metasurfaces,” Nat. Mater. **13**(2), 139–150 (2014).
23. Y. Gorodetski, G. Biener, A. Niv, V. Kleiner, and E. Hasman, “Optical properties of polarization-dependent geometric phase elements with partially polarized light,” Opt. Commun. **266**(2), 365–375 (2006).
24. D. Lin, P. Fan, E. Hasman, and M. L. Brongersma, “Dielectric gradient metasurface optical elements,” Science **345**(6194), 298–302 (2014).
25. N. Yu, P. Genevet, M. A. Kats, F. Aieta, J.-P. Tetienne, F. Capasso, and Z. Gaburro, “Light propagation with phase discontinuities: generalized laws of reflection and refraction,” Science **334**(6054), 333–337 (2011).
26. M. I. Shalaev, J. Sun, A. Tsukernik, A. Pandey, K. Nikolskiy, and N. M. Litchinitser, “High-Efficiency all-dielectric metasurfaces for ultracompact beam manipulation in transmission mode,” Nano Lett. **15**(9), 6261–6266 (2015).
27. G. Li, M. Kang, S. Chen, S. Zhang, E. Y. Pun, K. W. Cheah, and J. Li, “Spin-enabled plasmonic metasurfaces for manipulating orbital angular momentum of light,” Nano Lett. **13**(9), 4148–4151 (2013).
28. F. Bouchard, I. De Leon, S. A. Schulz, J. Upham, E. Karimi, and R. W. Boyd, “Optical spin-to-orbital momentum conversion in ultra-thin metasurfaces with arbitrary topological charges,” Appl. Phys. Lett. **105**(10), 101905 (2014).
29. E. Karimi, S. A. Schulz, I. De Leon, H. Qassim, J. Upham, and R. W. Boyd, “Generating optical orbital angular momentum at visible wavelengths using a plasmonic metasurface,” Light Sci. Appl. **3**(5), e167 (2014).
30. M. Pu, X. Li, X. Ma, Y. Wang, Z. Zhao, C. Wang, C. Hu, P. Gao, C. Huang, H. Ren, X. Li, F. Qin, J. Yang, M. Gu, M. Hong, and X. Luo, “Catenary optics for achromatic generation of perfect optical angular momentum,” Sci. Adv. **1**(9), e1500396 (2015).
31. D. Hakobyan, H. Magallanes, G. Seniutinas, S. Juodkazis, E. Brasselet, “Tailoring orbital angular momentum of light in the visible domain with metallic metasurfaces,” Adv. Optical Mater. **4**(2), 306 (2015).
32. M. Q. Mehmood, S. Mei, S. Hussain, K. Huang, S. Y. Siew, L. Zhang, T. Zhang, X. Ling, H. Liu, J. Teng, A. Danner, S. Zhang, and C.-W. Qiu, “Visible-frequency metasurface for structuring and spatially multiplexing optical vortices,” Adv. Mater. **28**(13), 2533–2539 (2016).
33. L. Marrucci, C. Manzo, and D. Paparo, “Optical spin-to-orbital angular momentum conversion in inhomogeneous anisotropic media,” Phys. Rev. Lett. **96**(16), 163905 (2006).
34. S. Slussarenko, A. Murauski, T. Du, V. Chigrinov, L. Marrucci, and E. Santamato, “Tunable liquid crystal q-plates with arbitrary topological charge,” Opt. Express **19**(5), 4085–4090 (2011).
35. D. Giovannini, E. Nagali, L. Marrucci, and F. Sciarrino, “Resilience of orbital-angular-momentum photonic qubits and effects on hybrid entanglement,” Phys. Rev. A **83**(4), 042338 (2011).
36. V. D’Ambrosio, N. Spagnolo, L. Del Re, S. Slussarenko, Y. Li, L. C. Kwek, L. Marrucci, S. P. Walborn, L. Aolita, and F. Sciarrino, “Photonic polarization gears for ultra-sensitive angular measurements,” Nat. Commun. **4**, 2432 (2013).

37. T. Bauer, P. Banzer, E. Karimi, S. Orlov, A. Rubano, L. Marrucci, E. Santamato, R. W. Boyd, and G. Leuchs, "Observation of optical polarization Möbius strips," Science **347**(6225), 964–966 (2015).
38. L. Yan, P. Gregg, E. Karimi, A. Rubano, L. Marrucci, R. W. Boyd, and S. Ramachandran, "Q-plate enabled spectrally diverse orbital-angular-momentum conversion for stimulated emission depletion microscopy," Optica **2**(10), 900 (2015).
39. M. Khorasaninejad and K. B. Crozier, "Silicon nanofin grating as a miniature chirality-distinguishing beam-splitter," Nat. Commun. **5**, 5386 (2014).
40. A. Arbabi, Y. Horie, A. J. Ball, M. Bagheri, and A. Faraon, "Subwavelength-thick lenses with high numerical apertures and large efficiency based on high-contrast transmitarrays," Nat. Commun. **6**, 7069 (2015).
41. A. Arbabi, Y. Horie, M. Bagheri, and A. Faraon, "Dielectric metasurfaces for complete control of phase and polarization with subwavelength spatial resolution and high transmission," Nat. Nanotechnol. **10**(11), 937–943 (2015).
42. M. Khorasaninejad, A. Ambrosio, P. Kanhaiya, and F. Capasso, "Dispersion-compensated meta-holograms based on detour phase," Sci. Adv. **2**, e1501258 (2016).
43. R. C. Devlin, M. Khorasaninejad, W.-T. Chen, J. Oh, and F. Capasso, "Broadband high-efficiency dielectric metasurfaces for the visible spectrum," Proc. Natl. Acad. Sci. U.S.A. **113**(38), 10473–10478 (2016).
44. M. V. Berry, "Optical vortices evolving from helicoidal integer and fractional phase steps," J. Opt. A, Pure Appl. Opt. **6**(2), 259–268 (2004).
45. J. Leach, E. Yao, and M. J. Padgett, "Observation of the vortex structure of a non-integer vortex beam," New J. Phys. **6**, 71 (2004).
46. J. B. Götte, S. Franke-Arnold, R. Zambrini, and S. M. Barnett, "Quantum formulation of fractional orbital angular momentum," J. Mod. Opt. **54**(12), 1723–1738 (2007).
47. S. S. R. Oemrawsingh, A. Aiello, E. R. Eliel, G. Nienhuis, and J. P. Woerdman, "How to observe high-dimensional two-photon entanglement with only two detectors," Phys. Rev. Lett. **92**(21), 217901 (2004).
48. S. S. R. Oemrawsingh, X. Ma, D. Voigt, A. Aiello, E. R. Eliel, G. W. 't Hooft, and J. P. Woerdman, "Experimental demonstration of fractional orbital angular momentum entanglement of two photons," Phys. Rev. Lett. **95**(24), 240501 (2005).
49. M. Menro, J. Liu, W. Rudolph, D. Ristau, and K. Starke, "Scaling laws of femtosecond laser pulse induced breakdown in oxide films," Phys. Rev. B **71**(11), 115109 (2005).
50. J. B. Götte, K. O'Holleran, D. Preece, F. Flossmann, S. Franke-Arnold, S. M. Barnett, and M. J. Padgett, "Light beams with fractional orbital angular momentum and their vortex structure," Opt. Express **16**(2), 993–1006 (2008).

1. Introduction

A helical mode of light is an optical field whose azimuthal phase evolution around the propagation axis (z) has the form $\exp[i\ell\varphi]$, φ being the azimuthal angle and ℓ (an integer) called topological charge of the beam. The wavefront of a helical mode of charge ℓ is constituted by $|\ell|$ helical surfaces twisted together, whose handedness is set by the sign of ℓ, resulting in a topological singularity (optical vortex), along the propagation axis [1]. Such vortex beams carry an average of $\ell\hbar$ orbital angular momentum (OAM) per photon [2,3]. Additionally, circularly polarized modes carry a spin angular momentum of $\pm\hbar$ per photon, depending on the polarization handedness. Such beams are central to the field of singular optics [4] and have found numerous applications such as optical trapping [5] where the angular momentum is a powerful manipulation tool to spin the trapped object [6,7] as well as to control its orientation [8].

The characteristic screw-type dislocation of a helical mode can be imposed on the wavefront of a propagating beam by means of different devices, for example, pitch-fork holograms [9,10] or cylindrical and axicons lenses and reflectors [11,12]. Additionally, helical modes can be also produced by exploiting the geometrical phase (also known as Pancharatnam-Berry (PB) phase) [13–15], to create inhomogeneous gratings for the wavefront reshaping [16,17]. In these spin-orbital angular momentum converters (SOC) the OAM of the vortex beam is coupled with the spin angular momentum of the illuminating light: switching the handedness of the illuminating beam polarization (spin angular momentum) flips the handedness of the vortex (orbital angular momentum). Locking the OAM to the spin angular momentum has unique applications in quantum computing and communications, allowing high dimensionality encoding of quantum units [18] and fast switching related to the modulation of the incident polarization of light [19–21].

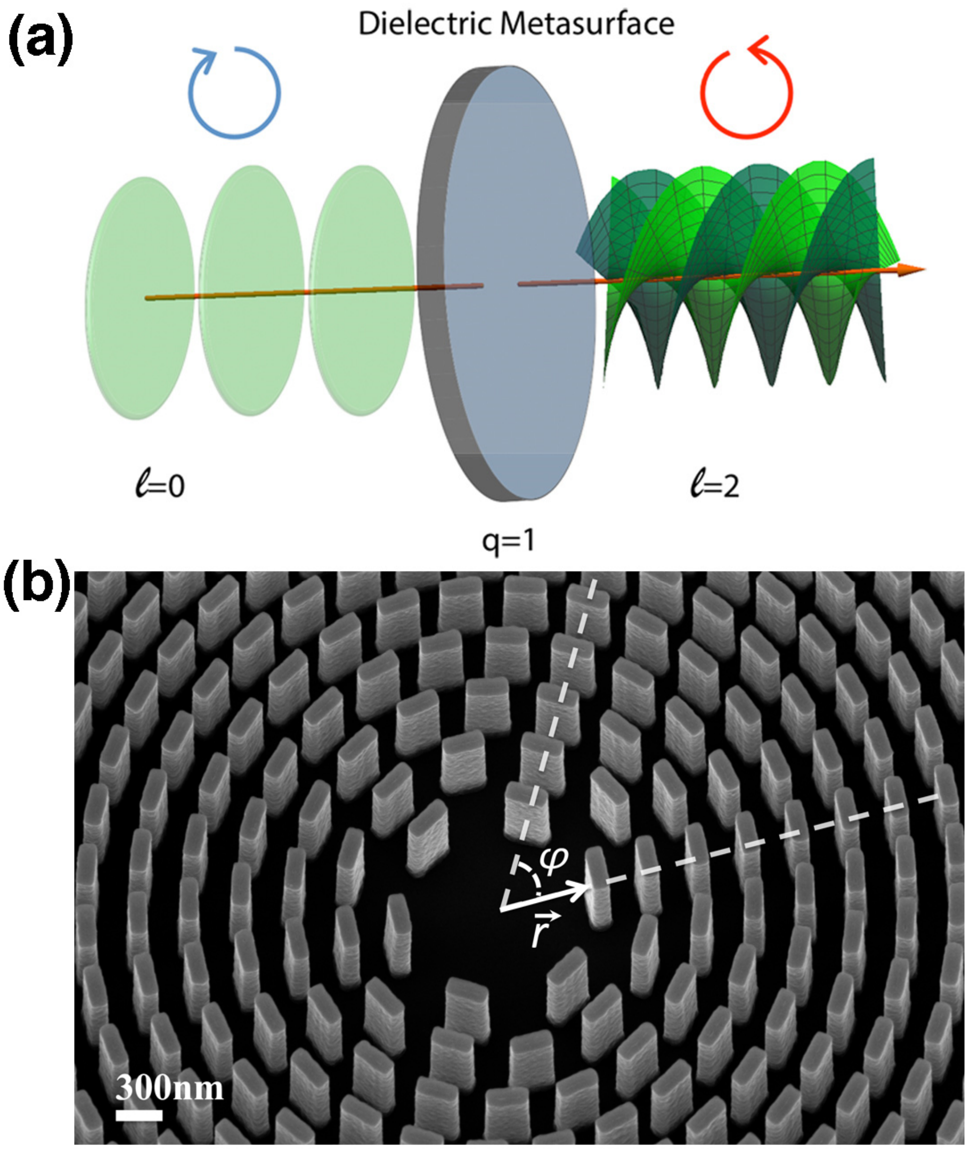

Fig. 1. (a) Schematic of the working principle of a spin-orbital angular momentum converter. A left circularly polarized beam with plane wavefront is turned into a right circularly polarized helical mode. In this representation the helical mode has a topological charge equal to 2, as the wavefront is composed of two intertwined helices. (b) Angled-view SEM image of one of our devices ($q = 1$) showing the orientation of the TiO_2 nanofins on the glass substrate, φ is the azimuthal angle and $|r|$ is the distance from the center.

More recently, the wavefront manipulation allowed by metasurfaces [22] has been used to produce a variety of PB optical elements, e.g., lenses [23,24] and vortex beam generators in the near-infrared [25,26]. Similar approaches have allowed working with visible light although with low transmission efficiency in the bluest part of the spectrum [27–32]. To date, the most versatile spin-orbital angular momentum converters for visible light are the liquid crystal devices developed by Marrucci et al. in 2006 and known as q-plates [33]. They have found numerous applications in quantum optics although they are limited by degradation effects and resolution in defining the extent of the topological singularity region [34–38].

2. Nanostructured dielectric Spin-to-Orbital angular momentum Converter

In order to describe some general features of a SOC based on PB phase, it is useful to define the orientation angle $\alpha(x, y)$ of the optical axis (fast or slow) of each element of the device in the transverse plane (x-y plane). Regardless of the constituents, if each element imposes a π phase delay between the field transverse components, an incident uniform left-circularly polarized beam $E_{in} = E_0 \times [1, i]$ is turned into the beam $E_{out} = E_0 \exp[i2\alpha(x, y)] \times [1, -i]$ that is right-circularly polarized with a geometrical phase $2\alpha(x, y)$ in the transverse plane. Analogously to what reported in the first description of a q-plate [33], if the azimuthal variation of the angle α in the PB-device follows the relation $\alpha = q\varphi + \alpha_0$, the incident wave front is then turned into a helical wavefront composed of $2|q|$ intertwined helical surfaces which carries an orbital angular momentum $\ell = \pm 2q\hbar$, where the sign depends on the handedness of the incident light polarization (α_0 is a constant). For instance, if $q = 1$ and the incident light is left-circularly polarized (spin angular momentum of $+\hbar$), the out coming light is right-circularly polarized (spin angular momentum of $-\hbar$) with an OAM per photon of $2\hbar$ and zero net angular momentum transferred to the device (Fig. 1(a)). For $q \neq 1$ there will be a net angular momentum exchange with the PB-device to preserve the total angular momentum of the system.

In our devices, as compared to previous work on metallic metasurface q-plates [28,29], the constitutive elements (nanofins) are subwavelength dielectric resonators [39–42] made of TiO_2 [43] (Appendix). Each nanofin is 250 nm long, 90 nm wide and 600 nm tall. The radial distance between two fins is of 325 nm (Fig. 1(b)). Figures 2(a) and 2(b) show the scanning electron microscope (SEM) images of the devices with $q = 0.5$ and $q = 1$ ($|\ell| = 1$ and $|\ell| = 2$ respectively). The insets of Figs. 2(a) and 2(b) show the devices as imaged in cross-polarization. The first polarizer sets the incident polarization direction. Each nanofin works as a half waveplate for the incident light: the nanofin rotates the incident polarization according to its orientation. The cross polarizer after the metasurface filters out the polarization opposite to that of the light incident on the metasurface thus creating $4q$ intensity lobes in the camera image.

In order to fully characterize the vortex beams, we used a Mach-Zehnder interferometer as shown in Fig. 2(c). In this configuration, the source beam (a solid-state laser emitting at 532 nm with power lower than 2mW) is split in two linearly polarized beams by means of a 50/50 beam splitter. Half of the light (upper arm of the interferometer) passes through a quarter waveplate (QWP1) to produce a circularly polarized beam incident on the device. The vortex beam created by the device then passes through a polarization filter made of a quarter waveplate (QWP2) and a linear polarizer (LP2) in cross-polarization with respect to QWP1. This polarization filter is used to eliminate non-converted light passing through the device (Appendix). The reference beam propagates in the lower arm of the interferometer and passes through a half waveplate (HWP) to acquire the same polarization of the helical mode in port 1 (as well as in port 2). This maximizes the intensity modulation (thus the contrast) in the interference pattern.

Figure 2(d) shows the intensity distribution of a vortex beam with $|\ell| = 1$, generated by the device in Fig. 2(a), in a transverse plane (plane of the camera at port 1 of the setup) at about 45 cm from the device exit plane, when the reference beam is blocked. Figure 2(f) shows the intensity profile for the vortex beam with $|\ell| = 2$ generated by the device of Fig. 2(b). The four insets of Figs. 2(e) and 2(g) show the intensity patterns produced in the plane of the camera by interfering the vortex beam with the reference beam. Such interference experiments are widely used to reveal phase singularities [4]. The pitchfork-like interference is obtained when a vortex beam and a Gaussian beam interfere with an angle between their propagation axes, which sets the fringe spacing. If the vortex beam is collinear with the reference beam from the lower arm of the interferometer, a spiral is obtained as an interference pattern, with the number of arms equal to the topological charge of the vortex beam. The handedness of the incident circularly polarized light sets the orientation of the pitchforks and spirals.

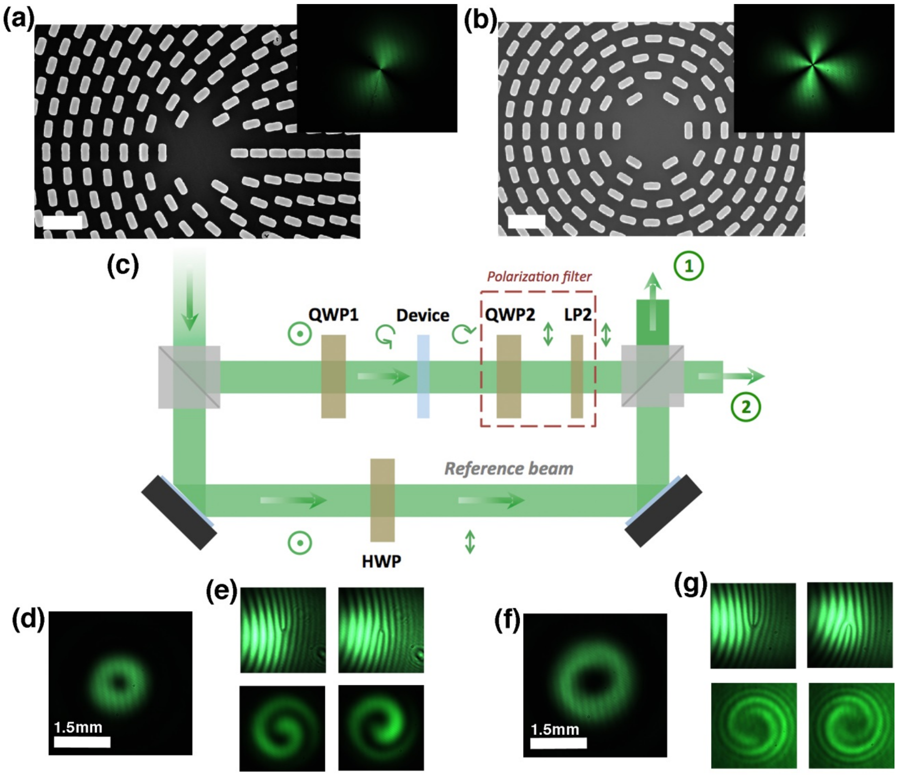

Fig. 2. (a) and (b), Scanning electron microscope image of TiO_2-based spin-orbital angular momentum converters with $q = 0.5$ and $q = 1$ respectively (scale bar = 650 nm). The insets show the devices observed in cross-polarization at the design wavelength of 532nm. (c), Sketch (top view) of the interferometric setup used to characterize the devices. The interference of the helical mode and the reference beam was monitored at port 1 by means of a CCD. The polarization state of the beam after each optical element is sketched. The laser polarization is linear and perpendicular to the optical table. Light becomes circularly polarized after the first quarter waveplate (QWP1). The helical mode generated by the device is circularly polarized with opposite handedness. The helical mode after the polarization filter (QWP2 followed by LP2) is linearly polarized parallel to the optical table. The reference beam in the lower arm of the interferometer becomes also linearly polarized parallel to the optical table after passing through a half waveplate (HWP) that rotates the polarization direction by 90°. (d), Transverse intensity distribution of the vortex beam generated by the device of Fig. 2 (a). This beam has a topological charge equal to 1. (e), Interference patterns obtained with tilted reference beam (pitchforks) or collinear reference beam (spirals) in the setup of Fig. 2(c). The flipped features result from opposite handedness of the beam that illuminates the device. (f), (g), Same as (d) and (e) for the device in Fig. 2(b).

Figure 3 shows how our approach can be used to produce optical vortices with higher values of topological charge, $|\ell| = 5$ (Figs. 3(a)-3(d)) and $|\ell| = 10$ (Figs. 3(e)-3(h)). Each individual device is 500μm in diameter and all devices are on the same glass substrate of 1 inch diameter (Appendix). This allows mounting the device on standard opto-mechanical components and to select the desired topological charge just by translating the corresponding device into the laser beam path.

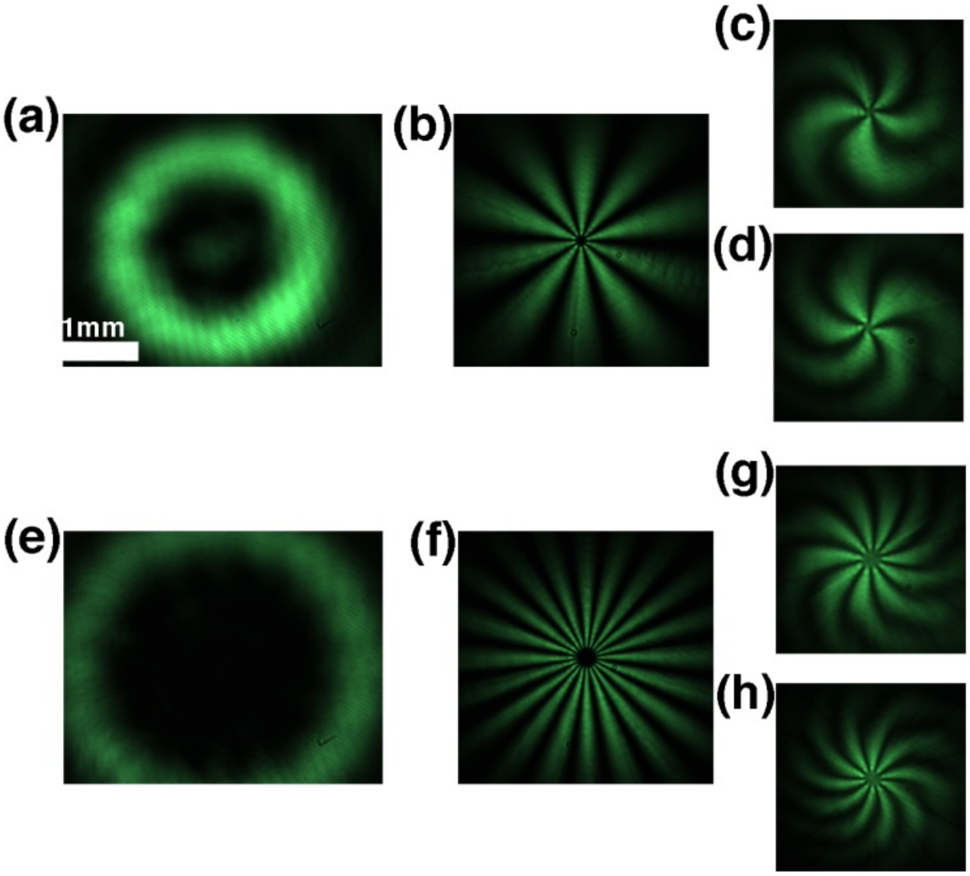

Fig. 3. Transverse intensity profile of a beam with topological charge 5 generated by means of our $q = 2.5$ spin-orbital angular momentum converter. (b), The $q = 2.5$ device imaged in cross-polarization. (c), (d), Images of the interference patterns obtained with a collinear reference beam (Fig. 2(c)) for incident left or right circular polarized light. (e), (f), (g), (h), Same as for (a), (b), (c), (d) for the topological charge 10 beam and the $q = 5$ device. Scale for (e) is same as shown in (a).

Another important feature of our devices is related to the localization of the beam singularity. The fabrication process is based on atomic layer deposition (ALD) and electron beam lithography (EBL) (Appendix). This guarantees high resolution and reproducibility, resulting in precise definition of the singularity region and improving the vortex beam quality. For example, the $q = 0.5$ device has a singularity region smaller than 3μm (Appendix).

In our devices we reached absolute efficiencies (the amount of light from the illuminating beam that is actually converted into the helical mode while also accounting for absorption and reflection from the device/substrate) of 60% (Appendix). Since TiO_2 is ideally transparent at these wavelengths and the nanofins are only 600 nm in height, this measured efficiency is limited mainly due to reflections at the air-substrate and substrate-metasurface interfaces and error between the fabricated and designed nanofin dimensions. Thus this device provides a substantial improvement in efficiency as compared to previous metallic metasurface q-plate devices with conversion efficiencies of 8.4% at an operating wavelength of 780 nm [29]. The simulated phase delay between the x- and y-component of the electric field and resulting conversion efficiency as a function of wavelength are shown in Appendix E and while the efficiencies we reported here were for 532 nm illumination, high efficiencies can be achieved at any visible wavelength simply by re-optimizing the lengths and widths of the individual TiO_2 nanofins, as we showed in ref [43]. Finally, the fact that these devices are fabricated using lithography and etching allows many devices with different topological charge to be placed on a single substrate—this is not easily-achievable with liquid crystal devices.

3. Fractional and interlaced spin-to-orbital angular momentum converters

As a further demonstration of the versatility of our approach, we designed a SOC that produces a vortex beam with fractional topological charge. This is possible when a non-integer phase discontinuity is introduced in the azimuthal evolution of the helical mode. In this case, Berry described the optical vortex as a combination of integer charge vortices with a singularity line in the transverse plane surrounded by alternating optical single charge vortices [44,45]. From a quantum optics point of view, the average angular momentum per photon has a distribution peaked around the nearest integer value of the topological charge and a spread proportional to the fractional part of the charge [46]. We fabricated a SOC producing a 6.5 topological charge vortex beam. Figure 4(a) shows the intensity distribution of the resulting helical mode at about 55μm from the device plane (Appendix) and Fig. 4(b) shows pitchfork-like interference obtained in the Mach-Zehnder configuration of Fig. 2(c). The phase singularity line predicted for such vortices is evident. The interference pattern (Fig. 4(b)) also shows the line of alternating vortices (single line pitchforks) along the singularity line. For half odd-integer values of the OAM, two helical modes with same OAM but phase singularities lines with a relative π orientation are orthogonal [45]. This has been used, for instance, to observe high-dimensional photon entanglement [47,48].

Our approach to SOC enables a new and unique feature, the generation of collinear beams from a single device with arbitrary and different OAM. In contrast, a detuned q-plate (i.e., a q-plate with phase delay not equal to π) can only produce a beam with OAM of 2q and a 0th order Gaussian beam with zero OAM, which is unconverted light.

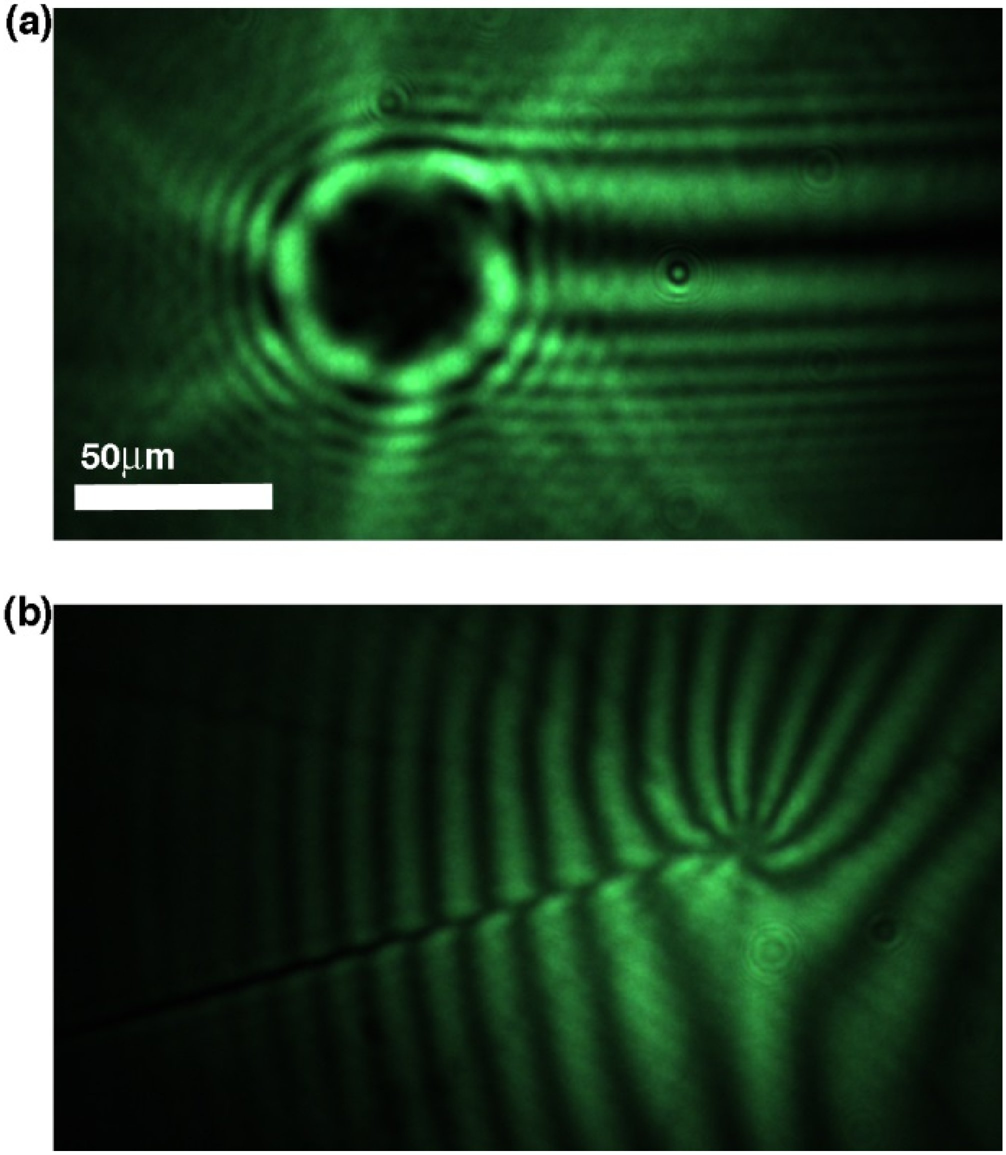

Fig. 4. (a), Transverse intensity distribution of a beam with topological charge 6.5 at 55µm from the device exit plane. (b), Interference pattern arising from the interference with a reference beam at oblique incidence. The resulting pitchfork pattern shows the singularity line surrounded by alternating single charge vortices, a characteristic feature of fractional helical modes. The direction of the singularity line in (a) and (b) is the same although in these figures they are on opposite directions due to the camera orientation during the experiment.

To demonstrate this concept, we designed an interlaced $q = 2.5$ and $q = 5$ device (Fig. 5(a)). Two metasurfaces with different azimuthal patterns are interleaved by placing the nanofins at alternating radii. Although they have different topological charges ($|\ell| = 5$ and $|\ell| = 10$), the beams emerge collinearly from the device, interfering in the plane transverse to the propagation direction. Figures 5(b) and 5(c) show the intensity patterns recorded in transverse planes (far from the device) for opposite handedness of the incident light. It is evident that the two interference patterns are flipped according to what is expected for beams with opposite topological charges. Figures 5(c) and 5(d) show the calculated interference patterns of two collinear helical modes of topological charges 5 and 10 with opposite handedness. These interference patterns are close to what we found experimentally if we assume for the charge 5 beam a Rayleigh range three times greater than for the charge 10 beam. In the calculations this accounts for the different divergence of the two experimental beams. While the interlaced designs allow for multiple values of OAM to be imprinted on a single beam, the measured efficiency for the interlaced device is 20%, which is less than the single topological charge. This drop in efficiency results from the spatial multiplexing of two devices—the period of each individual device is doubled leading to higher orders of diffraction.

It is important to note that each nanofin in our device has two interfaces, glass-TiO_2 and air-TiO_2. Illuminating one side or the other, as in Fig. 5(f), does not alter the phase delays imposed by the nanofins (Appendix) but only slightly affects light coupling into the latter, due to the different reflectance of the air-TiO_2 and glass-TiO_2 interfaces. We measured a small decrease (< 5%) in the device efficiency when illuminating from the air-side, due to the larger refractive indices difference with TiO_2.

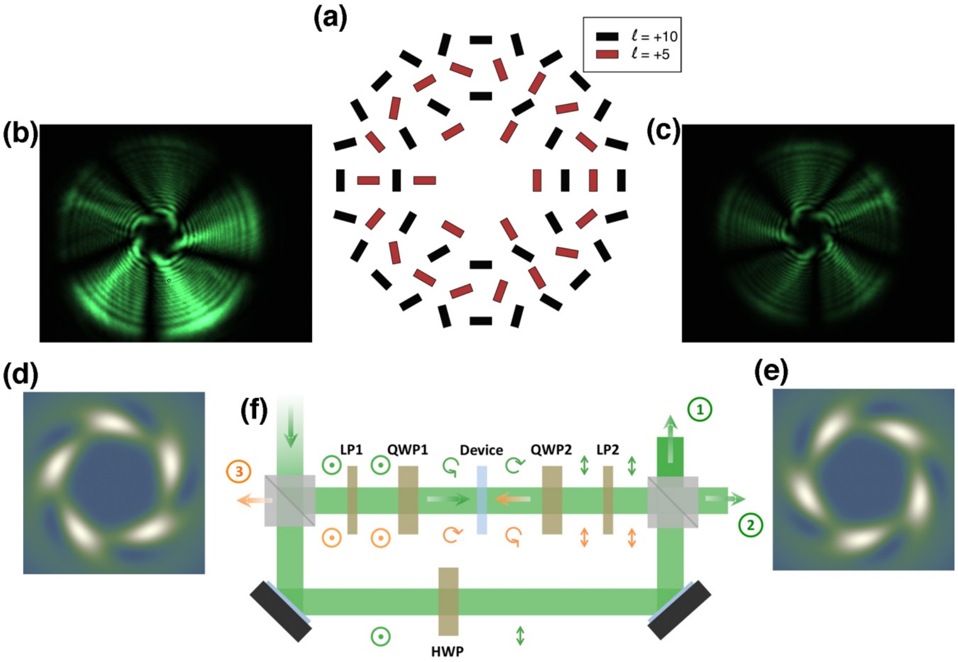

Fig. 5. (a) Schematic of the nanofins azimuthal distribution in the inner part of metasurface device with interleaved patterns that generate collinear beams having topological charges $|\ell| = 5$ and $|\ell| = 10$. The device has a 500 µm diameter and contains more than 700 interleaved radial rows of nanofins. (b), (c), Transverse intensity distributions of the light emerging from the metasurface for opposite handedness of the incident light. (d), (e), Simulated intensity patterns for collinear 5 and 10 topological charge beams. (f), Sketch of the setup that allows illumination of the transparent devices from the glass and air side simultaneously with circularly polarized beams of opposite handedness. In this case, there are two light beams, whose power can be made equal by suitably balancing the two arms, circularly polarized with opposite handedness that simultaneously illuminate the device from opposite sides at normal incidence. In this configuration, the helical modes propagating towards optical port 2 and 3 have also opposite wave-front handedness. This setup was also used to obtain the intensity distributions of Figs. 5(b) and 5(c).

4. Conclusions

In the setup of Fig. 5(f), the beams illuminating the sample from opposite interfaces have opposite handedness. The double-face characteristic of our devices together with the illumination configuration of Fig. 5(f) allows one to simultaneously generate similar beams with opposite topological charges. This configuration was also used to obtain the intensity distributions of Fig. 5(b) and 5(c) representing the helical modes at optical ports 3 and 2 respectively.

Although we limited our interlaced design to two collinear beams, it is possible to produce three or more collinear vortices simultaneously as well as $+\ell$ and $-\ell$ collinear vortices (Appendix). This can find important applications in entanglement and quantum computing experiments. Moreover, the quantum description of a device simultaneously generating co-propagating vortex beams with different topological charges has never been investigated and represents a stimulating direction for future work. Finally, we expect good tolerance to heating since TiO_2 has an intensity damage threshold of 0.5 J/cm^2 in the femtosecond regime [49]; thus we envision using such devices for non-linear optics with pulsed lasers. We actually exposed one of our devices to a CW laser (532nm wavelength) with a power of 1W over the device area for 5 hours without observing any change in the device efficiency and beam quality.

In summary we have demonstrated that the interaction of light with designer metasurfaces can lead to the generation of complex wavefronts characterized by arbitrary integer and fractional topological charges and co-propagating beams with different orbital angular momenta. Our approach represents a major advance in design with respect to liquid crystals devices and as such has considerable potential in several areas of optics and photonics, ranging from quantum information processing to optical trapping and complex beam shaping.

Appendix A. The device constitutive element (nanofin)

The individual units of the devices demonstrated in the main text are TiO_2 nanofins, shown schematically in Figs. 6(a) and 6(b). These units were fabricated using electron beam lithography and atomic layer deposition of TiO_2 onto the electron beam resist, as was previously described by our group in reference [43]. The low temperature deposition yields amorphous TiO_2 that has minimal surface roughness, which minimizes scattering losses. Additionally the TiO_2 has a high refractive index, ranging from 2.64 at λ= 400 nm to 2.34 at λ = 700 nm and a bandgap of 3.46 eV, which lies outside of the visible portion of the spectrum. At the design wavelength (λ= 532 nm) for the devices described in the main text the measured TiO_2 refractive index is 2.43. This value of refractive index is sufficiently high to confine the incident light to individual nanostructures and the bandgap occurring in the ultraviolet ensures there is no absorption at visible wavelengths.

In order to impose a geometric phase on an incident light field while maximizing the efficiency [16], the nanofins must possess structural birefringence so that a π phase delay can be imparted on orthogonal components of the incident electric field (the x- and y-components of the electric field in the example shown here). With our nanofins this birefringence is implemented for a fixed height (h), Fig. 6(a), by varying the length (L) and width (W), Fig. 6(b). In this way, different each component of light experiences a different effective refractive index, i.e. the nanofins are acting as waveplates with a fast and slow axis.

As stated in the main text, a waveplate with a spatially-varying fast axis (Pancharatnam-Berry phase optical elements [PBOE]), can impart a geometry-dependent phase on an incident circularly polarized light field. The imparted phase arises due to rotation of individual elements causing incident light to traverse two different paths on the Poincaré sphere. When the paths form a closed loop, the phase of the exiting light is then equal to half the solid angle of the loop. For our nanofins, which act as half waveplates, spatial rotation of each nanofin by an angle α (Fig. 6(b)) allows us to imprint the geometric phase and ultimately achieve the phase profile for producing a vortex beam, $\alpha = q\varphi + \alpha_0$.

The geometric parameters of the fins, W and L, were determined using 3-dimensional finite difference time domain simulations (Lumerical). At a fixed height of 600 nm, W and L were allowed to vary so that for an incident wavelength of $\lambda = 532$ nm, there would be a π phase shift between the x- and y-components of the incident electric field. From this optimization, it was found that fins with W = 90 nm and L = 250 nm provided the desired phase shift as can be seen from the simulated electric field profiles in Fig. 6(c) [43].

Appendix B. Device fabrication

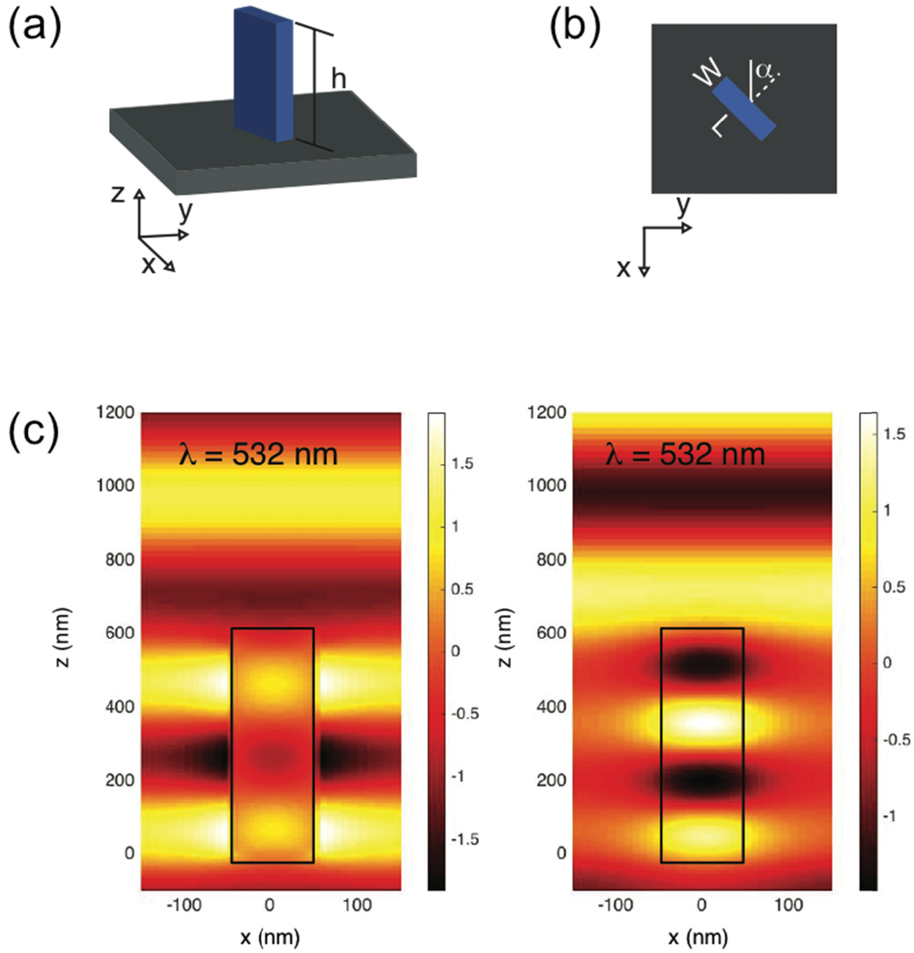

Fig. 6. (a) Perspective view of a single nanofin that makes up our devices. The fabrication process produces fins with a given height, *h*, which is 600 nm for all devices. (b), Top view of the TiO_2 nanofin. The fins are designed with width, *W*, length, *L* and rotation angle with respect to the x-axis, *α*. The length and width of the nanofin sets the relative phase delay between orthogonal components of an incident electric field and the rotation provides the geometric phase. (c), Cross section through the width of a single nanofin, showing the simulated electric field components. The real part of the x-component (left) and y-component (right) of the electric field. At the design parameters of $W = 90$ nm, $L = 250$ nm, $h = 600$ nm, there is a π phase delay between the x- and y-components.

All devices used were fabricated on a fused silica substrate. Resist was spun at 1750 rpm in order to achieve a thickness of 600 nm. The resist was then baked at 180° C for 5 mins. The patterns were exposed using electron beam lithography (ELS-F125, Elionix Inc) and developed in o-Xylene for 60 s. For the ALD (Savannha, Cambridge Nanotech) of TiO_2, TDMAT precursor was used to avoid chlorine contamination and the system was left under continuous 20 sccm flow of N_2 carrier gas and maintained at 90° C throughout the process. Reactive ion etching was carried out on Unaxis ICP RIE with a mixture of Cl2 and BCl3 gas (3 and 8 sccm, respectively) at a pressure of 4 mTorr, substrate bias of 150 V and ICP Power of 400 W. The samples were finally placed in 2:1 sulfuric acid:hydrogen peroxide to remove any residual electron beam resist.

Appendix C. The Device

The devices described in the main text have been designed such that they can be easily integrated into manual or automatic positioning systems. Figure 7(a) shows a 1-inch fused silica substrate that has been patterned with TiO_2 metasurfaces. The sample sits on a manual translation stage but automatic translation stages could be used for faster switching. Such design allows SOCs producing different topological charges to be arrayed on a single device at regular distances, (Fig. 7(b)) and easy switching between an output beam with a desired topological charge.

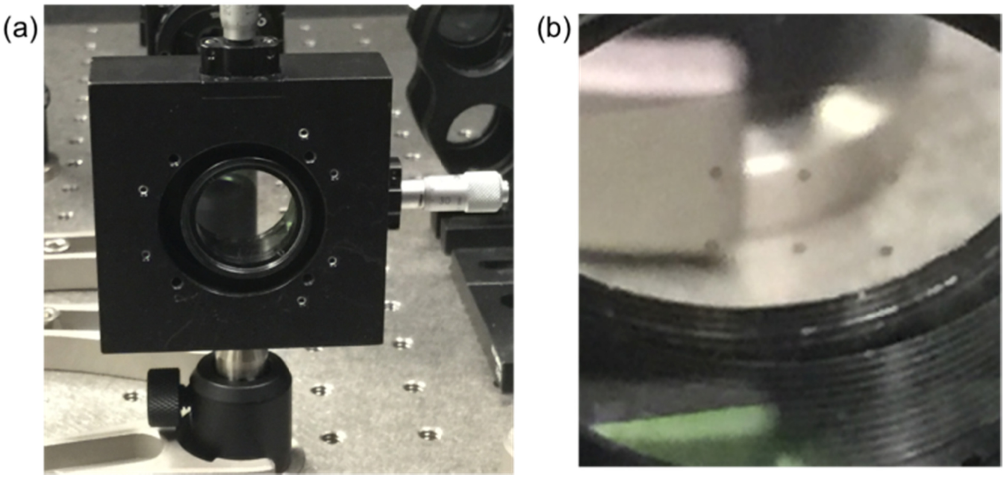

Fig. 7. (a) The devices are produced on a circular 1-inch diameter fused silica wafer, which is then integrated into a commercial opto-mechanic component. (b), Magnified view of the 1-inch wafer in (a) showing six devices on the same substrate. The devices are placed in a rectangular array across the wafer, which allows easy selection of a device by moving it into the illuminating beam path.

Appendix D. Imaging at a distance from the device exit plane

In order to produce an image of the transverse light distribution at different distances from the sample plane, the upper arm of the interferometer was slightly modified. In particular the source beam was focused on the device by means of a 75mm aspherical lens. The light emerging from the device was then collected by means of a 4X infinity corrected microscope objective. The objective has 0.10 NA and works in confocal configuration with the aspheric lens. The sample is mounted on a translation stage that allows changing the distance from the objective. This configuration has been used, for instance, in the figure below that shows a fractional optical vortex at 55µm from the device exit plane. Figure 8 shows the image of the center of the $q = 0.5$ device when the device plane is in focus. This image is what is sometimes referred to as near-field image although does not contain any near-field component. The image shows that the singularity localization in the device plane is smaller than 3μm. In ref [28] device singularities of 750 nm are reported. The physical dimension of the device singularity (region with no nanofins) in these metasurface devices is 1200 nm, however the fabrication technique used here can produce devices with controlled vacancies (i.e., lack of nanofin) on the order of the unit cell dimension of a few hundred nanometers. As pointed out in [28] this is an advantage of the metasurface q-plates.

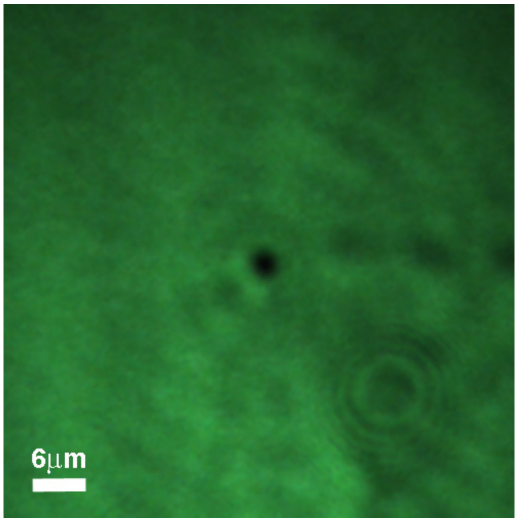

Fig. 8. Image of the singularity region of a $q = 0.5$ device.

Appendix E. Device efficiency and conversion over the visible range

The polarization filter of Fig. 2(c) is used to eliminate the light that passes unperturbed through the device. This light has opposite handedness with respect to the helical mode and is absorbed by the polarization filter. It is known that when a waveplate that introduces a phase delay Γ between the transverse field components is illuminated by circularly polarized light, the out coming field has two components with opposite handedness [38]:

$$E_{out} = \frac{1}{2}\left(1+e^{-i\Gamma}\right)\sigma + \frac{1}{2}\left(1-e^{-i\Gamma}\right)e^{i2\alpha}\sigma^{-} \tag{1}$$

The term weighted by the $\frac{1}{2}\left(1+e^{-i\Gamma}\right)$ has the same handedness (σ) of the incident light, the term weighted by $\frac{1}{2}\left(1-e^{-i\Gamma}\right)$ has opposite handedness (σ^{-}) with respect to the incident field and acquires an extra phase term $e^{i2\alpha}$, where α is the orientation of the plate axis (each nanofin in our devices).

In some experiments in literature, the percentage of light with σ^{-} handedness ($\left|\frac{1}{2}\left(1-e^{-i\Gamma}\right)\right|^{2} = \sin^{2}\frac{\Gamma}{2}$) is reported as the beam purity since represents the fraction of total outcoming light converted into the desired helical mode to the unconverted light [31]. This feature, though, does not account whatsoever for the device transmittance since the purity can be close to 100% even if the transmittance is as low as a few percent. This is a particularly important point for communication and quantum optics applications where for high fidelity systems it is necessary that both the transmission efficiency and conversion efficiency of the transmitted light be maximized.

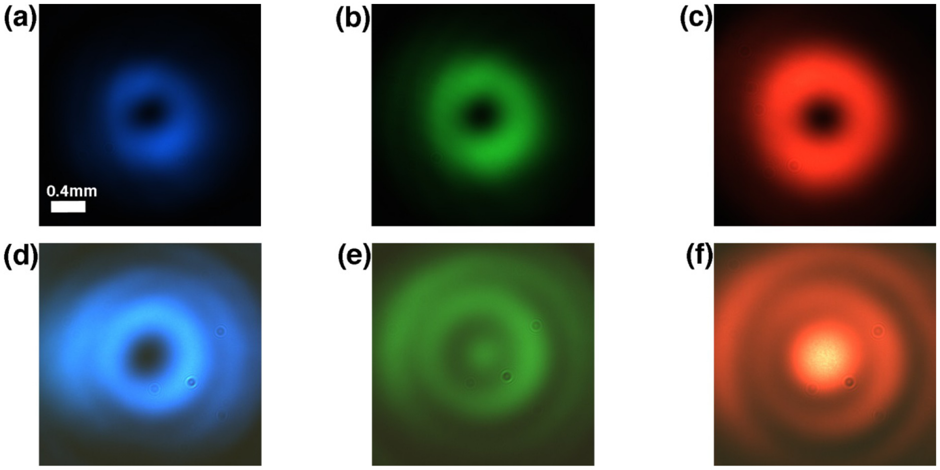

Fig. 9. Images of the donut beams at three different wavelengths from a supercontinuum laser: 480 nm ((a) and (d)), 550 nm ((b) and (e)) and 633 nm ((c) and (f)). The images in the upper row are taken with the setup of Fig. 2 (c) while the images in the lower row are taken by removing the polarization filter. The scale bar of 0.4mm in Fig. 9 applies to all the panels.

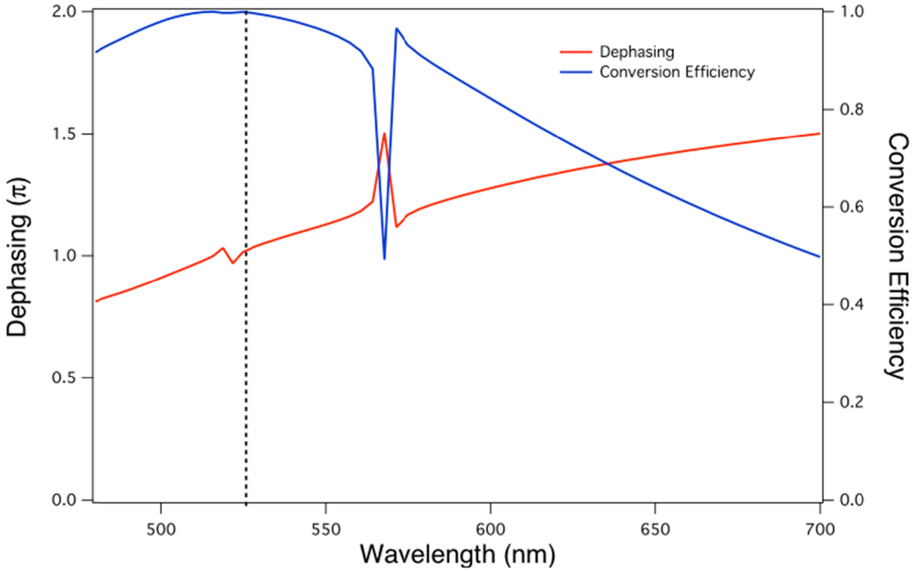

Fig. 10. Nanofin dephasing and conversion efficiency as a function of wavelength. Simulated dephasing between the x- and y- components of the electric field after passing through the nanofins (red line) and the resulting ideal conversion efficiency (blue line).

We designed our devices for a π phase delay at λ=532 nm. The transmittance of TiO_2 in the visible is greater than 80%. The efficiency that we report in our paper is the amount of light that is converted in a helical mode with respect to the light incident on the device. We think that this value (experimentally measured to be up to 60%) is more useful for practical uses since it takes into account the fact that in a real device with discrete features like our TiO_2 nanofins, a certain amount of light just passes through non-modulated. Furthermore, in a real experiment there are also reflections at the interfaces. These effects are all included in the figure of merit that we measured.

Actually, an inhomogeneous grating design [24] with densely packed grooves can in principle allow reducing the amount of light that passes through the device without acquiring the proper phase delay. This could result in even higher efficiency values at the designed wavelength. However, such design is limited to cylindrically symmetric structures like those necessary to generate a topological charge 2 vortex and cannot be applied to generate arbitrary vortex beams.

The wavelength dependence of the phase delay Γ imposed by the constitutive elements of spin-orbital momentum converters based on metasurfaces limits the efficiency bandwidth of such devices. The actual phase delay is equal to π only at the designing wavelength. The farther the wavelength is from the designed wavelength the larger the amount of unperturbed light, according to Eq. 1. However, the Pancharatman-Berry phase is path-length independent and does not change with the wavelength of the incident light. Figure 9 shows a single charge helical mode obtained at different wavelengths from a supercontinuum laser with our 532nm optimized device.

The simulated phase shift between the x- and y- components of the electric field after passing through the nanofin and resulting as a function of wavelength is shown in Fig. 10. As can be seen from the figure, the conversion peaks around the design wavelength (532 nm) and is lower away from the design wavelength since the nanofin no longer acts as a half wave plate. Changing the design parameters of the nanofins would allow optimizing the device operation at other wavelengths [43].

Appendix F. Fractional Vortex in far-field

Figure 11 shows the light distribution of the fractional 6.5 vortex beam at the camera plane, about 45cm from the device exit plane. The singularity line visible at 55μm from the device (Fig. 4 (a)) is no longer visible [50].

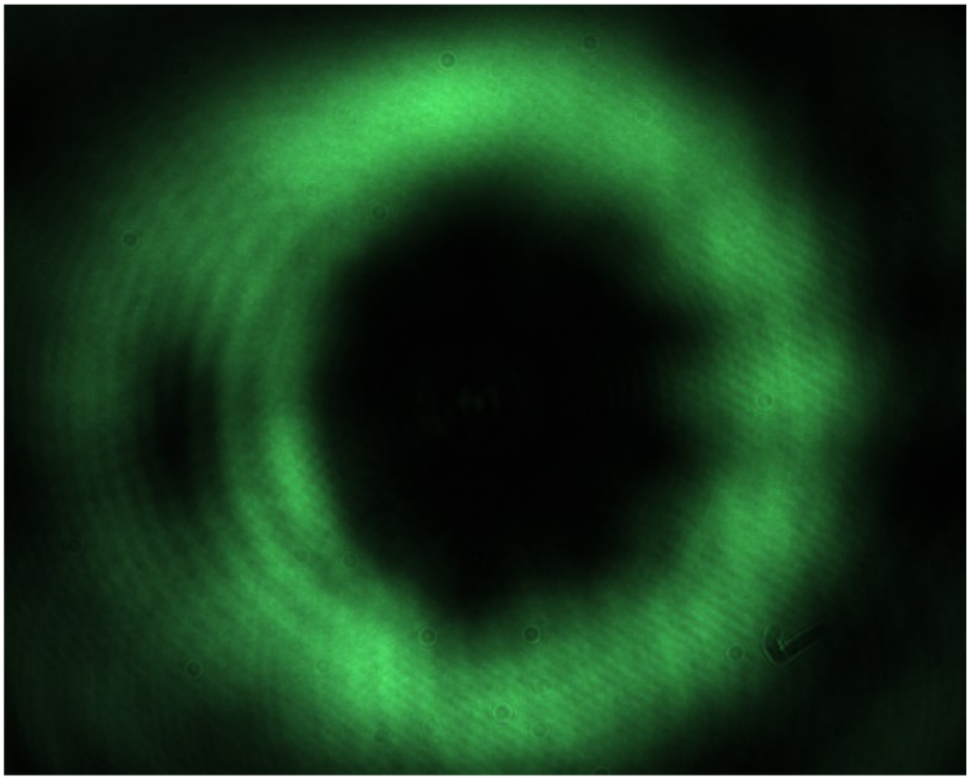

Fig. 11. Far-field image of the 6.5 topological charge vortex beam.

Appendix G. Plus/Minus topological charge interlaced device

In addition to the interlaced +5,+10 device, we have also produced a device with the same magnitude but opposite sign of topological charge (Fig. 12).

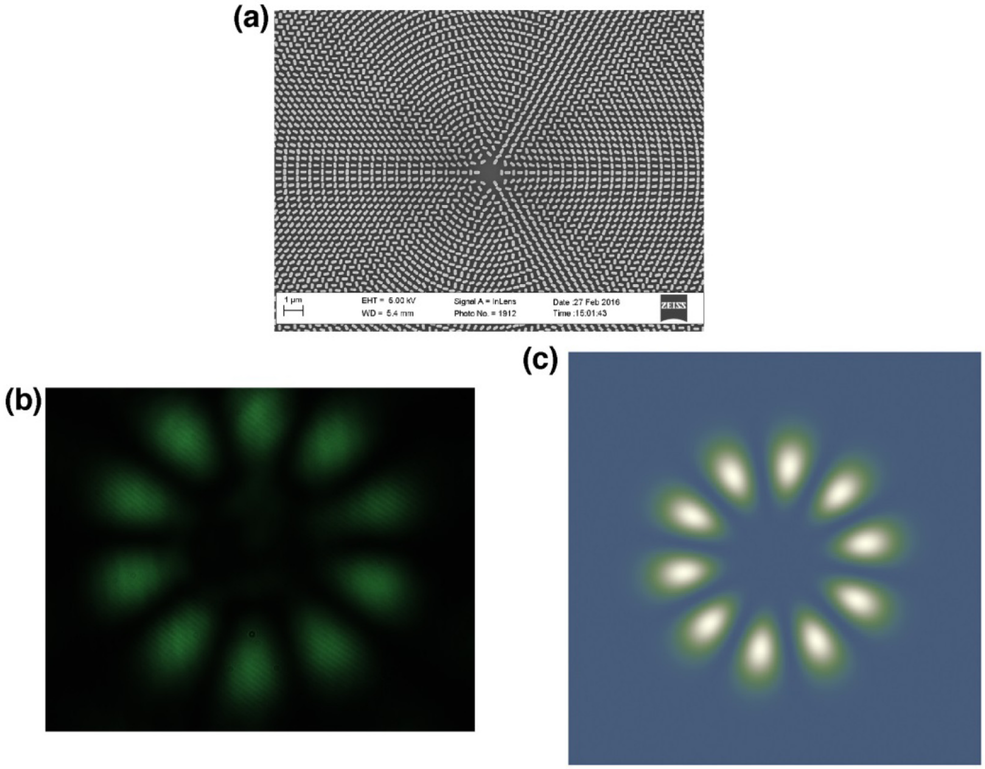

Fig. 12. (a), Scanning Electron Microscopy micrograph of an interlaced $q = \pm 2.5$ device. (b), light distribution at 45 cm from the device exit plane. (c), simulated interference pattern of two collinear beams with topological charges + 5 and −5.

Funding

R.C.D is supported by a Draper Laboratory Fellowship. We also acknowledge financial support from Air Force Office of Scientific Research (AFOSR) contract FA9550-14-1-0389 and FA9550-16-1-0156); Charles Stark Draper Laboratory Contract SC001-0000000959 and from Thorlabs Inc. Fabrication was performed at the Harvard University Center for Nanoscale Systems (CNS), a member of the National Nanotechnology Coordinated Infrastructure (NNCI), which is supported by the National Science Foundation under NSF award no. 1541959. CNS is a part of Harvard University.